Sustainable Cities and Society 53 (2020) 101972

Contents lists available at ScienceDirect

Sustainable Cities and Society

journal homepage: www.elsevier.com/locate/scs

Influences of urban spatial form on urban heat island effects at the community level in China

Andong Guo[a], Jun Yang[a,b,*], Xiangming Xiao[c,d], Jianhong Xia (Cecilia)[e], Cui Jin[a], Xueming Li[a]

[a] Human Settlements Research Center, Liaoning Normal University, 116029 Dalian, China
[b] Jangho Architecture College, Northeastern University, Shenyang 110169, China
[c] Department of Microbiology and Plant Biology, Center for Spatial Analysis, University of Oklahoma, Norman, OK 73019, USA
[d] Ministry of Education Key Laboratory of Biodiversity Science and Ecological Engineering, Institute of Biodiversity Science, Fudan University, Shanghai 200433, China
[e] School of Earth and Planetary Sciences (EPS), Curtin University, Perth 65630, Australia

ARTICLE INFO

Keywords:
Urban heat island
Land surface temperature
Spatial form
Spatial autocorrelation
Spatial regression model
Dalian city

ABSTRACT

Owing to increasing population densities and impervious surface areas, heat island effects increasingly dominate urban environments and hinder sustainable development. The urban spatial form plays an important role in mitigating urban heat islands. Taking Ganjingzi District, Dalian, as an example, this study considered urban spatial form at the community scale using spatial autocorrelation and spatial regression methods to explore 2003–2018 spatial and temporal differentiation characteristics and driving factors of Land Surface Temperature (LST). The LST of each community showed a gradually increasing trend; high values (> 30°C) were concentrated in central and eastern areas; low values were (< 25°C) was concentrated in the south and west. LSTs were influenced by spatial variables (e.g., land use); however, building form was only weakly related to LST. The global autocorrelation Moran's *I* value for LST exceeded 0.7, indicating strong positive correlation in terms of spatial distribution. H-H and L-L LISA values were distributed in central and southern areas, respectively. The spatial error model (SEM) was a better fit than the spatial lag (SLM) or ordinary least squares models (OLS) and was used to explore these relationships. This study focuses on community surface temperature and hopes to provide a valuable reference for community planning, resource allocation and sustainable development.

1. Introduction

The 21st century has been referred to as "the century of urbanization", in which the city is a complex system produced by interactions between socioeconomics and the environment. Cities dramatically change ecosystems, land use, biodiversity, and water, which can cause various negative effects for people (e.g., traffic congestion, air pollution, and deteriorated ecological environments (Bolund & Hunhammar, 1999; He, 2018; KIM, 1992; Ren, Ng, & Katzschner, 2011; Tan et al., 2010). Urban heat islands (UHI) are caused by rapid increases in population density and impervious surfaces accompanied by reductions in green space that result in locally elevated land surface temperatures in urban areas (Howard, 1818; Oke, 1982; Wang, Zeng, & Karl, 1990). Cities have two-dimensional (e.g., land use/cover and landscape) and three-dimensional (e.g., structures and vegetation) features that change significantly during rapid urbanization and increases rates of heat absorption; as a result, UHIs are a prominent feature of urban climates (Stone & Rodgers, 2001; Son & Thanh, 2018; Wang, Ma, Ding, & Liang, 2018; Zullo, Fazio, Romano, Marucci, & Fiorini, 2019). In the context of current global temperature rise, high population agglomeration and rapid urban spread, urban heat islands have seriously affected the quality of daily life of residents and the sustainable development of cities. Therefore, exploring the spatial and temporal pattern of urban thermal environments and the impact of urban spatial forms on the thermal environment has important value for mitigating urban heat islands, which are of widespread concern for planners and communities (Imhoff, Zhang, Wolfe, & Bounoua, 2010; Rizwan, Dennis, & Chunho, 2008; Yang et al., 2017).

Land surface temperature (LST) refers to the temperature of the Earth's surface measured by its thermal radiation. Recent developments in remote sensing technology have provided perspectives and techniques for studying UHI using LST measurements (Sobrino, Li, Stoll, & Becker, 1996; Voogt & Oke, 2003). Stewart and Oke (2012) proposed 17 climate zone types based on urban surface cover and three-

* Corresponding author at: Human Settlements Research Center, Liaoning Normal University, Dalian 116029, China.
E-mail addresses: Gandong_GIS@163.com (A. Guo), yangjun@lnnu.edu.cn (J. Yang), xiangming.xiao@ou.edu (X. Xiao), c.xia@curtin.edu.au (J. Xia (Cecilia)), cuijin@lnnu.edu.cn (C. Jin), lixueming999@163.com (X. Li).

https://doi.org/10.1016/j.scs.2019.101972
Received 9 July 2019; Received in revised form 15 October 2019; Accepted 16 November 2019
Available online 18 November 2019

dimensional structures (structural and vegetation heights) as an effective way to measure urban thermal environments (Cai, Ren, Xu, Lau, & Wang, 2018; Yang, Jin et al., 2019). Simultaneously, multidisciplinary efforts among, for example, meteorology, geography, and urban planning, have merged urban big data with machine learning and deep learning, in order to expand and diversify the perspectives and methods used to study urban climate (Mirzaei, 2015; Ngie, Abutaleb, Ahmed, Darwish, & Ahmed, 2014; Yue, Liu, Fan, Ye, & Wu, 2012).

To date, research on UHI has mostly focused on data sources, unit selection, analytical methods, driving factors, mitigation measures, and effective simulation (Chen, Yang, & Zhu, 2014; Kong et al., 2017; Mirzaei & Haghighat, 2010; Shi, Katzschner, & Ng, 2018). Grid cells are often used for urban thermal environment research, mainly because surface temperature is based on remote sensing images (raster data). However, owing to the spatial resolutions of remote sensing images, the observed LST and the surface cover structure differ, and the relationship between them is masked. Therefore, choosing the appropriate analytic unit is important for studying the spatial characteristics of UHI (Li et al., 2011; Yang, Wang et al., 2019). Driving factors have mostly considered time and space, and temporal factors have focused on changes to LST during set periods (e.g., years, seasons, days, or nights; Mathew, Khandelwal, Kaul, & Chauhan, 2018; Peng et al., 2018; Qiao, Tian, & Xiao, 2013). Spatial factors include urban three-dimensional or two-dimensional spatial forms (Zhou & Chen, 2018). Multi-source remote sensing data, such as TM, ETM, OLI, MODIS, and AVHRR, have been used to invert LSTs (He, Zhao, Shen, Wang, & Li, 2019; Wang, Liang, & Meyers, 2008; Yang, Pu, Zhao, Huang, & Wang, 2011), the results are then combined with spatial scale and spatial regression methods (e.g., ordinary least squares, spatial metric modeling, or geographically-weighted regression analyses) to explore UHI spatial patterns and driving mechanisms (Dai, Guldmann, & Hu, 2018; Luo & Peng, 2016).

From a geographical perspective that values regional complexities, this study used spatial autocorrelation analysis and a spatial metric model combined with urban spatial form factors to identify and quantify the spatiotemporal patterns of UHI effects and causal factors. This study had a threefold objective: (1) to pre-process multi-temporal images using mono-window algorithms to invert LSTs and analyze the characteristics of the resulting spatiotemporal patterns; (2) to use spatial autocorrelation methods to explore spatial heterogeneity of surface temperatures; and (3) to use a community-based spatial regression method to explore the relationship between surface temperature and driving factors.

2. Materials and methods

2.1. Study area

Dalian City, China, is located at the southern tip of the Liaodong Peninsula on the coast of the Yellow Sea (Fig. 1). The city's major urban areas include Zhongshan District, Shahekou District, Xigang District, and Ganjingzi District. The city borders the sea on three fronts, enjoys moderate temperatures in winter and summer, and has a temperate monsoon climate. Ganjingzi District is Dalian City's link between the main urban areas and new urban areas. It is an important hub for railways, international airports, and seaports. Recent economic developments in Dalian City have led to major changes to urban spaces and land-use types, which has caused increasingly prominent UHI effects.

In China, regulatory planning is an important part of urban planning. The community unit is the basic unit for urban construction, rational planning of land use and development, and the allocation of public facilities. Thus, this study analyzed the spatiotemporal patterns of urban LSTs and their driving mechanisms at the community level. It then used those results to form recommendations for scientific decision-making during future urban planning.

2.2. Data

2.2.1. Data sources

Data used in this study included Landsat remote sensing images and 3D building information, the digital elevation model (DEM), nighttime lighting, roads, and land use. Landsat images were derived from the United States Geological Survey (USGS, https://earthexplorer.usgs.gov/) and the Geospatial Data Cloud of China (http://www.gscloud.cn/), and were mainly used for surface temperature inversion. The original downloaded data were resampled to 30 m. DEM data were from the Geospatial Data Cloud of China with a resolution of 30 m; and nighttime lighting image Data (Roga-1) were from Wuhan University (http://59.175.109.173:8888/); 3D building data and land use data were sourced from the Dalian Land Resources and Housing Bureau, where building data include information on building footprint and height. The data sources and their descriptions are given in Table 1.

2.2.2. Explanatory variables

Cities are complex dynamic systems influenced by social, economic, cultural, and policy characteristics; as such, while exploring the driving factors of UHIs many such factors should be considered (Qu, Zhu, Jia, & Lv, 2015; Wei, Yao, Chongyu, & Weijun, 2017; Zhao, Cai, Qiao, & Xu, 2016). Based on previous studies, this study explored the relationship between LST and driving factors from six perspectives: architectural form, land type, a landscape index, social economy, topography, and a remote sensing index (Azhdari, Soltani, & Alidadi, 2018; Mathew, Khandelwal, & Kaul, 2017; Yue, Xu, Tan, & Xu, 2007; Zhang, Estoque, & Murayama, 2017). From these six perspectives, a total of 16 influential variables were selected (Table 2 and Fig. 2).

At present, scholars focus on the selection of explanatory variables in two-dimensional space, but are limited in the acquisition of urban three-dimensional data; consequently, there are few analyses of the relationships among three-dimensional architectural forms and surface temperatures (Chun & Guldmann, 2014; Scarano & Mancini, 2017; Zakšek, Oštir, & Kokalj, 2011). This study selected building density and the sky view factor as explanatory variables. Remote sensing spectral indices have significant correlations with LST (Chen, Zhao, Li, & Yin, 2006; Feng et al., 2019), and the normalized difference vegetation index (NDVI), normalized difference built-up index (NDBI), and normalized soil brightness index (NDSI) were selected as explanatory variables. Different land cover types have different levels of heat absorption and heat dissipation, affecting regional surface temperature changes (Zhao, Jensen, Weng, & Weaver, 2018); we selected three indicators: construction land area percentage, forest grass land percentage, and water area percentage. Surface temperature is not only related to land cover type, but also to land cover morphological characteristics, spatial configuration and landscape pattern characteristics (Gage & Cooper, 2017). In this study, the patch density, aggregation index, and largest patch index were selected. The results of the index were obtained using the FRAGSTATS 4.3 software. At the same time, temperature is affected by altitude and landform, and the altitude and geomorphology affect the intensity of solar radiation, in turn affecting the spatial pattern of LST (Li, Zhao, Miaomiao, & Wang, 2010). Two indicators, the digital elevation model (DEM) and slope, were selected as explanatory variables. With the expansion of urban space, socioeconomic factors have a significant impact on urban microclimate. This study selected three indicators: road density, water distance, and nightlight. Among them, water distance refers not only to inland rivers but also to distance from the coastline.

There may be multiple collinearity problems in the selected variables. To avoid affecting the final regression results, we used the variance expansion factor (VIF) to identify collinearity (Table 3). When the VIF value is less than 7.5, there is no collinearity between the data. At the same time, it is judged whether data are normally distributed according to the standard deviation, skewness, and kurtosis of each variable. As can be seen from Table 3, the remote sensing spectral index

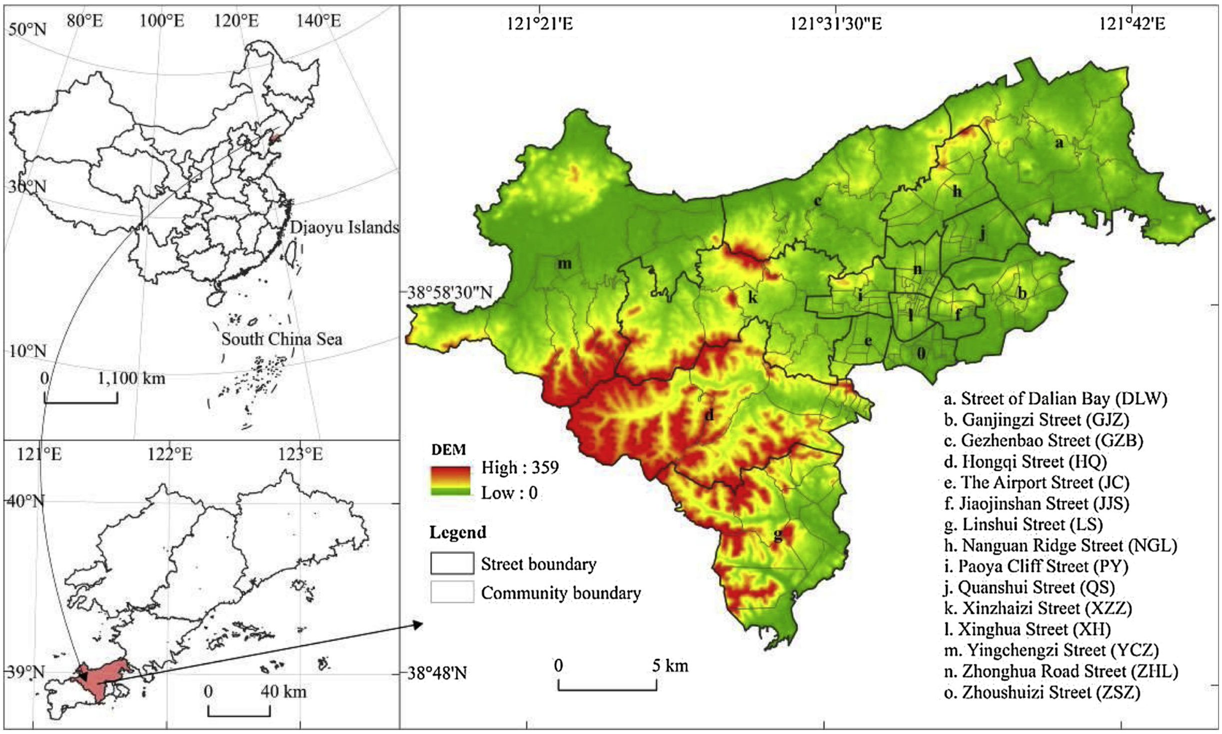

Fig. 1. Location and study area (Dalian City, China).

Table 1
Data sources.

Data source	Date/time	Spatial resolution (meters)	Description
Landsat 5 T M	25 Aug 2003, 10:06 UTC + 8	30	USGS (https://earthexplorer.usgs.gov/)
	06 Aug 2008, 10:15 UTC + 8	30	and Geospatial Data Cloud
Landsat 8 OLI	11 Aug 2013, 10:37 UTC + 8	30	(http://www.gscloud.cn/)
	09 Aug 2018, 10:34 UTC + 8	30	
DEM		30	Geospatial Data Cloud
Building data	2018		Dalian Land Resources and Housing Bureau
Night Lighting Image Data (Roga-1)	2018	130	http://59.175.109.173:8888/
Land use	2017	1:10000	Dalian Land Resources and Housing Bureau

Table 2
Explanatory variable description.

Type	Variables (abbreviated)	Formula	Description
Building form	Building density (BD)	Abi/Ai	The density of building in each community (Unit: %)
	Sky view factor (SVF)	See note	Used to measure the extent of 3D open space.
Land use	Percentage of construction land (PCL)	Acl/Ai	Percentage of land for construction in each community (Unit: %)
	Percentage of water (PW)	Aw/Ai	Percentage of water in each community (Unit: %)
	Percentage of woodland and grassland (PWG)	Awg/Ai	Proportion of forest land and grassland per community (Unit: %)
Landscape index	Patch density (PD)	——	Land use patch density per community (calculated by FRAGSTATS 4.3)
	Aggregation index (AI)	——	Aggregation index of land use in each community (calculated by FRAGSTATS 4.3)
	Largest patch index (LPI)	——	Largest patch index of land use in each community (calculated by FRAGSTATS 4.3)
Socio-economic	Nighttime light (NL)	__	Average night light intensity per community
	Road density (RD)	Ar/Ai	Percentage of road area per community (Unit: %)
	Distance to water (DisW)	__	Distance from the water (calculated by the EucDistance tool in ArcGIS 10.2) (Unit: m)
Terrain	DEM	__	Average DEM value per community (Unit: m)
	Slop	__	Average Slope for each community (calculated by the Slope tool in ArcGIS 10.2) (Unit: °)
Remote sensing index	Normalized Difference Vegetation Index (NDVI)	$\frac{\rho NIR - \rho RED}{\rho NIR + \rho RED}$	Average of NDVI per community
	Normalized Difference Build-up Index (NDBI)	$\frac{\rho SWIR - \rho NIR}{\rho SWIR + \rho NIR}$	Average of NDBI per community
	Normalized Difference Soil Brightness Index (NDSI)	$\frac{\rho RED - \rho GREEN}{\rho RED + \rho GREEN}$	Average of NDSI per community

Note: A_i represents the area of each community; A_{bi} represents the building area within each community; A_{cl}, A_w, A_{wg} represent the construction land, water area, forest and grass land area in the community; A_r represents the road area of each community; ρ_{RED}, ρ_{GREEN}, ρ_{NIR}, ρ_{SWIR} represent reflectance in the red, green, near-infrared, and mid-infrared bands. $SVF = \frac{1}{2\pi}\int_0^{2\pi}[\cos\beta\cos^2\varphi + \sin\beta\cos(\phi - \alpha)(90 - \varphi - \sin\varphi\cos\varphi)]d\phi$ (Yin, Yuan, Lu, Huang, & Liu, 2018).

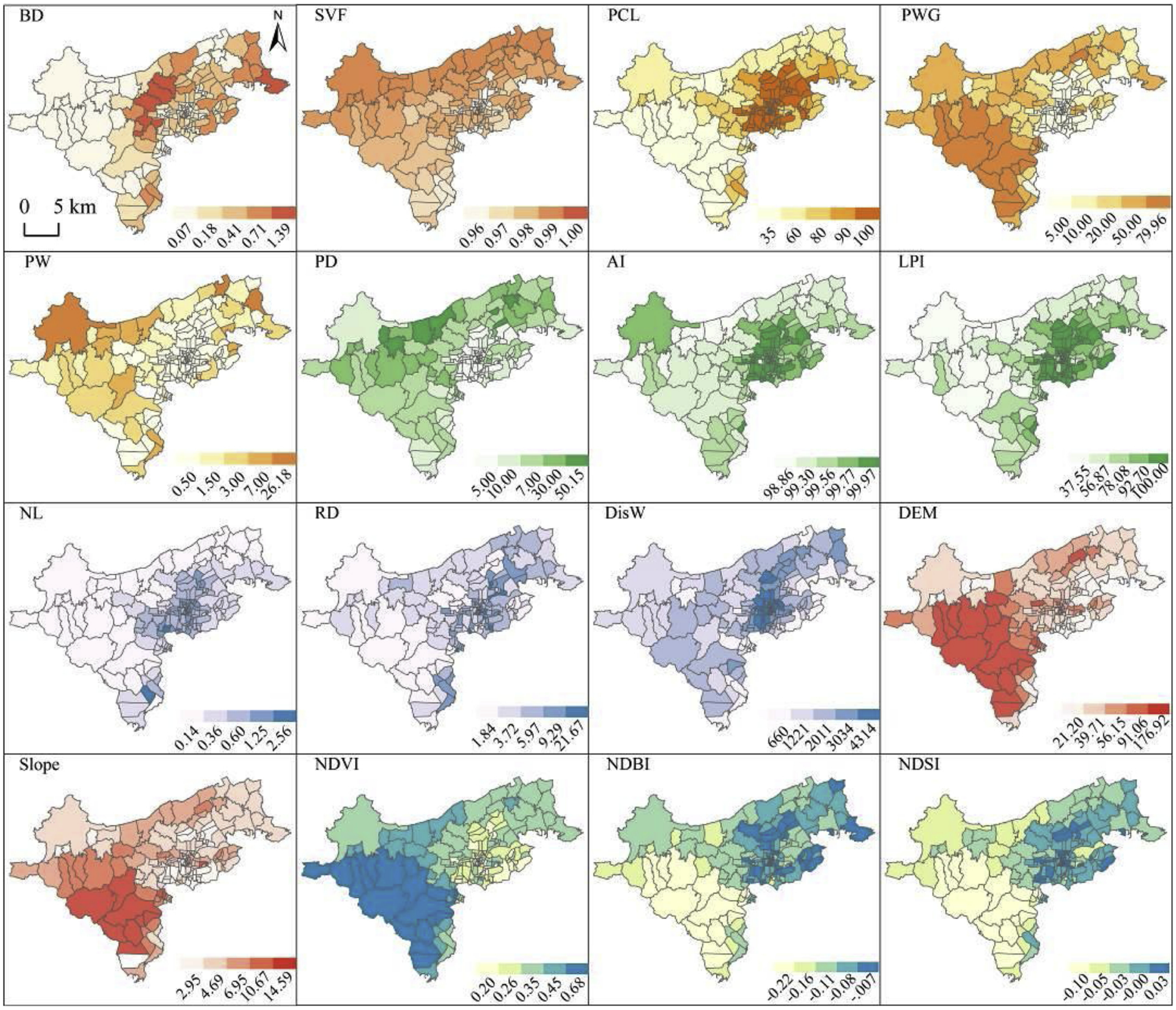

Fig. 2. Spatial variations of each independent variables used to correlate with LSTs.
BD = Building density; SVF = Sky view factor; PCL = Percentage of construction land; PW = Percentage of water; PWG = Percentage of woodland and grassland; PD = Patch density; AI = Aggregation index; LPI = Largest patch index; NL = Nighttime light; RD = Road density; and DisW = Distance to water.

has a higher VIF value. In order to make the data more consistent with a normal distribution and avoid the collinear problem, variables were processed logarithmically in the subsequent calculation process. After logarithmic processing, the data basically met a normal distribution and the VIF was less than 7.5.

β and α represent the surface slope angle and surface aspect; φ and ϕ represent the horizon angle and the azimuth direction.

Table 3
Descriptive statistics.

Type	V	Min	Max	Mean	SD	S	K	P	M	VIF
Building form	BD	0.00	1.39	0.17	0.23	2.80	9.28	−0.03	0.36	1.33
	SVF	0.94	1.00	0.99	0.01	−2.43	7.31	−0.23	0.37	1.49
Land use	PCL	5.20	100	76.32	27.42	−0.94	−0.34	0.86	0.58	10.70
	PWG	0.00	79.96	15.12	21.07	1.49	1.26	−0.82	0.42	16.46
	PW	0.00	26.18	1.05	3.03	5.63	38.32	−0.66	0.05	1.48
Landscape index	PD	0.48	50.15	10.83	9.28	1.61	2.88	−0.46	0.45	3.50
	AI	98.26	99.97	99.51	0.38	−1.12	0.93	0.67	0.64	7.59
	LPI	14.74	100.00	78.99	24.85	−0.91	−0.54	0.79	0.70	7.54
Socioeconomic	NL	0.02	2.56	0.42	0.36	2.63	12.52	0.51	0.50	1.63
	RD	0.00	21.68	4.36	3.30	1.63	4.42	0.45	0.32	1.49
	DisW	207.10	4314.25	1881.83	1118.63	0.37	−1.01	0.54	0.70	2.36
Terrain	DEM	6.94	176.91	46.43	31.62	1.43	2.28	−0.53	0.61	6.20
	Slope	1.11	14.59	5.01	2.88	1.59	2.39	−0.57	0.63	7.64
Remote sensing index	NDVI	0.12	0.68	0.30	0.12	1.20	1.03	−0.85	0.74	19.75
	NDBI	−0.33	−0.01	−0.12	0.06	−1.32	1.46	0.77	0.72	18.60
	NDSI	−0.18	0.03	−0.03	0.04	−1.71	2.74	0.81	0.71	19.41

Note: V = variable, SD = standard deviation, S = skewness coefficient, K = kurtosis coefficient, P = Pearson correlation coefficient, M = Moran's *I*.

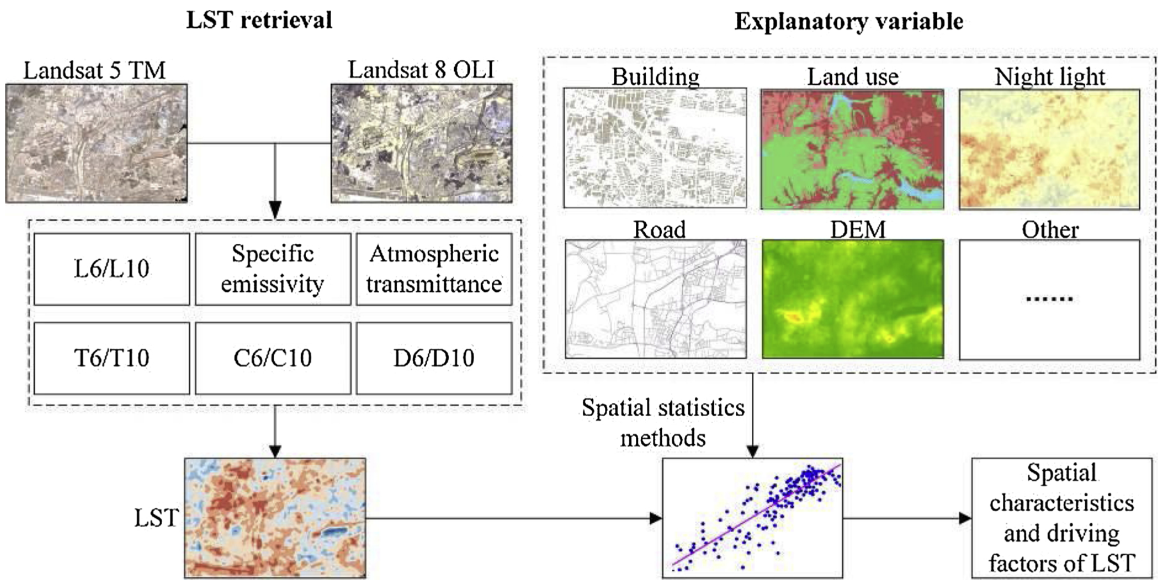

Fig. 3. Flow chart.
L6/L10 = radiation intensity value; T6/T10 = radiation brightness; C6/C10 and D6/D10 = intermediate variables from Eqs. (4) and (5).

2.3. Methods

This study was conducted at the community level using a mono-window algorithm to retrieve LSTs, followed by spatial autocorrelation and spatial statistical methods to investigate spatiotemporal characteristics and the driving factors of changes in them (Fig. 3). Firstly, through the preprocessing of Landsat remote sensing images for four time periods, the single-window algorithm was used to invert the surface temperature and analyze its temporal and spatial characteristics. Then, from the perspectives of architectural form, land use, landscape index, socio-economics, topography and the remote sensing spectral indices, a total of 16 variables were selected as explanatory variables. Finally, spatial statistical analysis methods (OLS, SLM, SEM) were used to investigate the relationship between surface temperature and driving factors, and the best method was selected by comparison of results.

2.3.1. LST data retrieval

Current practice for LST retrieval is based on remote sensing images from imaging sources, such as MODIS or Landsat, and mono-window algorithms, split-window methods, and atmospheric correction (Cristóbal et al., 2018; Dwivedi & Khire, 2018; Wan & Dozier, 1996). The mono-window algorithm is an LST retrieval algorithm proposed by Qin, Karnieli, and Berliner (2001) in response to the presence of just one thermal infrared band for (TM) data (Wang et al., 2015). Recently, many empirical analyses have been conducted using this method to achieve high levels of retrieval accuracy; this study used it to invert LSTs for analysis.

In the LST retrieval process, the thermal infrared band is first subjected to radiometric calibration, meaning that the digital number (*DN*) value is converted to the corresponding radiation intensity value L_λ (L_6/L_{10}), and then converted to the corresponding radiation brightness temperature value T_a (T_6/T_{10}). The L_6/L_{10} represents the radiation intensities of Band 6 and Band 10 in Landsat 5 T M and Landsat 8 OLI, respectively, and also applies to T_6/T_{10}. The relevant equations (1 and 2) are as follows:

$$L\lambda = Gain \times DN + Offset \tag{1}$$

$$T_a = \frac{K_2}{\ln\left(1 + \frac{K_1}{L\lambda}\right)} \tag{2}$$

where L_λ represents the radiation intensity value, T_a represents the brightness temperature, *Gain* represents the gain parameter, *Offset* represents the offset parameter, and the two parameters may be obtained in the downloaded remote sensing image MLT file. The $Gain$ = 0.055375 (Landsat TM) and 0.0003342 (Landsat OLI). The $Offset$ = 1.18243 (Landsat TM) and 0.1 (Landsat OLI). The *DN* represents the thermal infrared gray level value. For Landsat 5 T M remote sensing data, K_1 = 607.76 mW/(cm^2 sr μm) and K_2 = 1260.56 K. For Landsat 8 OLI remote sensing data, K_1 = 774.89 mW/(cm^2 sr μm) and K_2 = 1321.08 K.

The LSTs were obtained by using the T_a value from Equation 2 in Eq. (3) as follows:

$$Ts = \frac{(a(1 - C - D) + Ta(b(1 - C - D) + C + D) - DTb)}{C} - 273.15 \tag{3}$$

$$C = \varepsilon\tau \tag{4}$$

$$D = (1 - \tau)[1 + (1 - \varepsilon)\tau] \tag{5}$$

where T_s represents the actual LST; T_a represents the radiance value (K) from equations 1 and 2; T_b represents the atmospheric mean acting temperature (K); C and D are intermediate variables from Eqs. (4) and (5), respectively; and a and b are fitted coefficients based on thermal radiation intensity. When the temperature is between 0 °C and 70 °C, a = −67.355351 and b = 0.458606. The ε and τ are the surface emissivity and atmospheric transmissivity of the thermal infrared band, respectively (Valor & Caselles, 1996); ε represents surface emissivity based on NDVI and vegetation coverage (Singh, Kikon, & Verma, 2017; Sobrino, Jiménez-Muñoz, & Paolini, 2004) and τ represents atmospheric transmissivity calculated based on atmospheric parameters derived from NASA's website (http://atmcorr.gsfc.uasa.gov/).

2.3.2. Spatial autocorrelation

Based on Tobler's first geographic law, the closer the spatial distance is between objects, the greater the correlation between their attributes' values (i.e., the stronger the spatial dependence; (Tobler, 1970). In this study, the spatial heterogeneity of the LSTs was quantitatively measured and the global spatial autocorrelation coefficient (Moran's *I*) value was used (Li, Zhou, Ouyang, Xu, & Zheng, 2012) to assess it. Moran's *I* is a widely used global spatial autocorrelation statistic, calculated as shown in Eq. (6):

$$Moran'sI = \frac{n \sum_{i=1}^{n} \sum_{j \neq i}^{n} wij(xi - \bar{x})(xj - \bar{x})}{\sum_{i=1}^{n} \sum_{j \neq i}^{n} wij \sum_{i=1}^{n} (xi - \bar{x})^2} \tag{6}$$

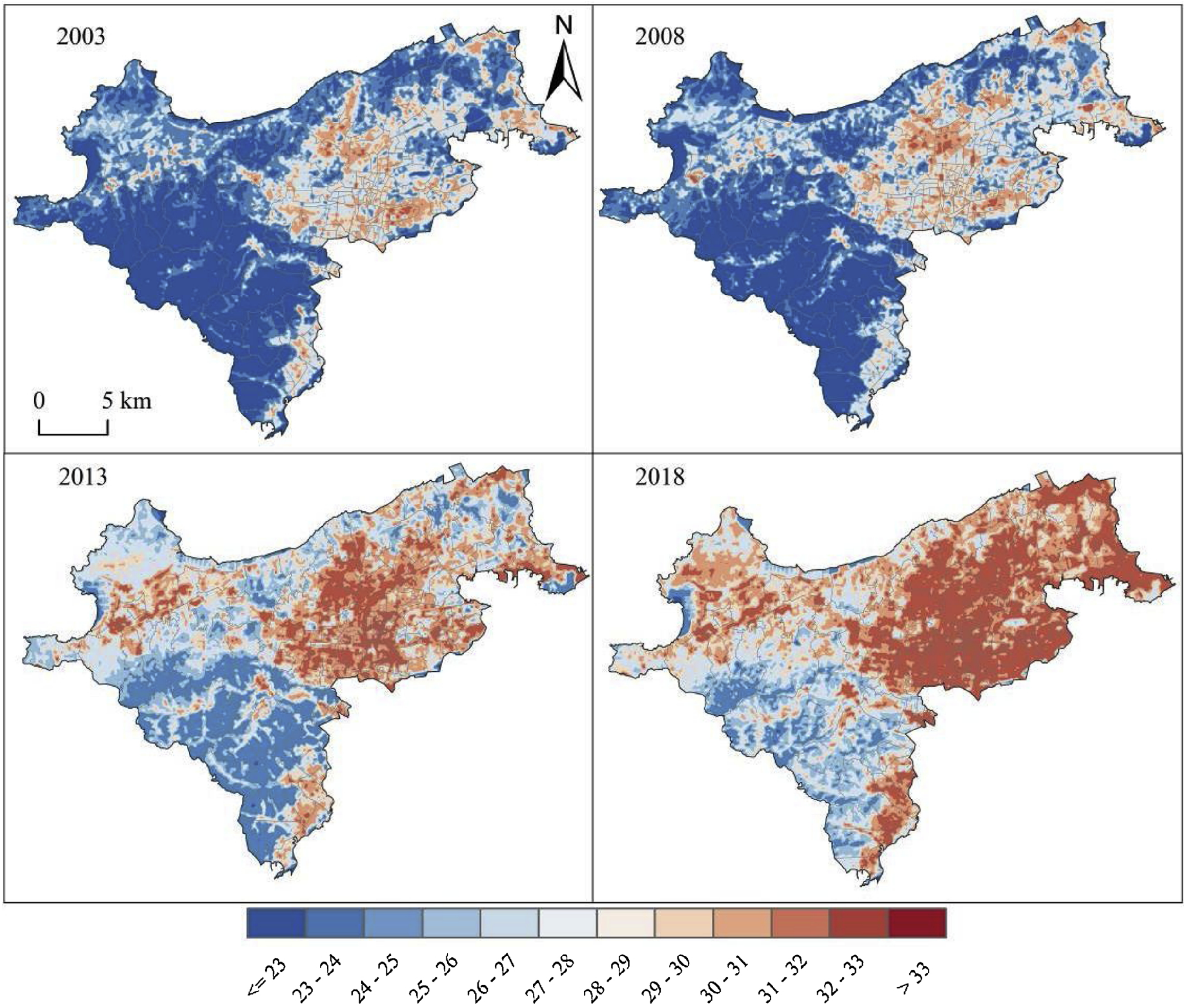

Fig. 4. Spatiotemporal land surface temperature (LST) patterns in 2003, 2008, 2013, and 2018.

$$LocalMoran'sI = \frac{n(xi - \bar{x})\sum_{j=1}^{n} wij(xj - \bar{x})}{\sum_{i=1}^{n}(xi - \bar{x})^2} \tag{7}$$

where x̄ x is the mean observed value for all n positions (areas), w_{ij} is the spatial weight matrix, and x_i and x_j represent the observed values for spatial positions i and j, respectively. The Moran's I index values range from -1 to 1; values less than zero imply negative correlations, values equal to zero indicate no correlation, and values greater than zero show positive correlations.

The local spatial autocorrelation index is often measured by the local Moran' I statistic (Eq. (7)), which is used to reveal the agglomeration and differentiation characteristics of geographic features in spatial locations; that is, to reflect the spatial correlation between the community and the neighboring community LST. Local Moran' I has a value range of $[-1, 1]$, and less than 0 indicates a negative correlation. The smaller the value, the more the similarity of the attribute values of the spatial unit and the adjacent unit (L-H aggregation, H-L aggregation); 0 means no correlation; greater than 0 means positive correlation, the larger the value, the higher the similarity of the attribute values of the unit and the adjacent unit (H-H aggregation or L-L aggregation).

2.3.3. Spatial regression models

This study focused on the influences of driving factors on the spatial characteristics of LSTs using spatial regression analysis. Spatial regression models effectively resolve problems of spatial dependence that cannot be handled by linear regression analysis. Common spatial regression models include the spatial lag model (SLM) and spatial error model (SEM). SLMs are mostly used to examine whether there is spatial diffusion or whether there are any spillover effects of the variables (Anselin & Rey, 1991; Song, Du, Feng, & Guo, 2014). The equation is as follows:

$$y = \rho Wy + X\beta + \varepsilon \tag{8}$$

where y is the dependent variable; X is the matrix of explanatory variables without an intercept term; β is the vector of the slope, reflecting the effect of the independent variable on the dependent variable, W_y is the spatial weight matrix. ε is a vector of random error terms. A statistically significant spatial autoregressive coefficient ρ means that there is significant spatial dependence between independent variables, and the magnitude of ρ reflects the extent of interaction between individual units, such as spatial diffusion or spatial spillover.

The SEM model formula is as follows:

$$y = X\beta + \lambda W\varepsilon + \mu \tag{9}$$

where λ represents the spatial autoregressive coefficient of the error term; W_ε represents the spatial weight matrix; and μ is a vector of the error terms. A statistically significant λ implies that some factors in the model are causing spatial autocorrelation between error terms.

The basic unit of spatial regression in this paper is the community. Therefore, the geographic adjacency method is used to set the weight of adjacent observations, and the SLM and SEM are implemented by GeoDa 1.12 software. In each regression model, the explanatory variables include 16 variables (Section 2.2.2). For verification and accuracy of the model, determination coefficient (R^2), Akaike Information Criterion (AIC), Log Likelihood (LogL), and Schwarz Criterion (SC) are often used to compare the results of the three global regression models. These four indicators represent relative measures of statistical fit; a better model will have higher R^2 and LogL values but lower AIC and SC values.

3. Analytical results

3.1. LST spatiotemporal characteristics

The spatial distributions of LSTs in Ganjingzi District for the four periods were obtained using the LST retrieval algorithm described in Section 2.3.1. Fig. 4 illustrates that, over 15 years, the LSTs of the communities gradually increased. Communities with high LSTs were mostly concentrated in the middle and eastern parts of the study area where the terrain is relatively low and land use is dominated by built-up areas. In the southwest, far from the Dalian City center, a relatively high mostly forested terrain exists with lower LSTs.

To further explore the spatiotemporal characteristics of the urban thermal environment, street-level spatial statistical analysis was performed for LST data (Fig. 5). The maximum, minimum, and mean values of the surface temperatures of the streets gradually increased. Among them, from the average surface temperature, high values mainly include Xinghua Street, Zhonghua Road Street, Zhoushuizi Street, and Paoya Cliff Street. Low values mainly include Yingchengzi Street and Xinzhaizi Street. From 2003–2018, the increase was larger. Xinghua Street, Zhonghua Road Street, and Paoya Cliff Street increased by 4.27 °C, 3.63 °C, and 3.62 °C, respectively. From the maximum and minimum surface temperature, maximum surface temperature mainly included Zhoushuizi Street, Zhonghua Road Street, and Xinghua Street; the 2018 LST values were 34.71 °C, 34.22 °C, and 35.02 °C, respectively. The minimum value was observed for Gezhenbao Street. The 2018 LST values of Yingchengzi Street and Lingshui Street were 25.96 °C and 25.80 °C, respectively.

3.2. LST spatial autocorrelation

To investigate LSTs' spatiotemporal characteristics in Ganjingzi District, spatial autocorrelation analysis assessed spatial heterogeneity. The Moran scatter plot represents the correlation between the LST normalized value and its spatial lag value by a two-dimensional graph, which in turn explains the instability of the local space. Fig. 6 shows that the Moran's *I* of LSTs in the four periods were 0.76, 0.76, 0.74, and 0.73. These consistently high values indicate significant positive spatial correlations (i.e., strong spatial aggregation).

To further reveal the characteristics of the variation in communities' LSTs' spatial autocorrelations, the LSTs' local indicators of spatial association (LISA) values for the four periods were calculated (Fig. 7). The LST spatial distribution patterns of the four periods were generally stable. High value (H-H) areas were mainly in the central region and included the Zhonghua Road, Jiaojinshan, Zhoushuizi, Airport, and Xinghua subdistricts. Low value (L-L) areas were mainly in the southwest and included the Hongqi, Lingshui, and Yingchengzi subdistricts. Low value areas surrounded primarily by high value (L-H) areas were spatially scattered and mostly located in the central region.

3.3. Regression results and influential factors

To ascertain a preliminary forecast for the explanatory variables and to compare with the spatial regression model, OLS was used for model estimation. The LST values of communities in 2018 comprised the

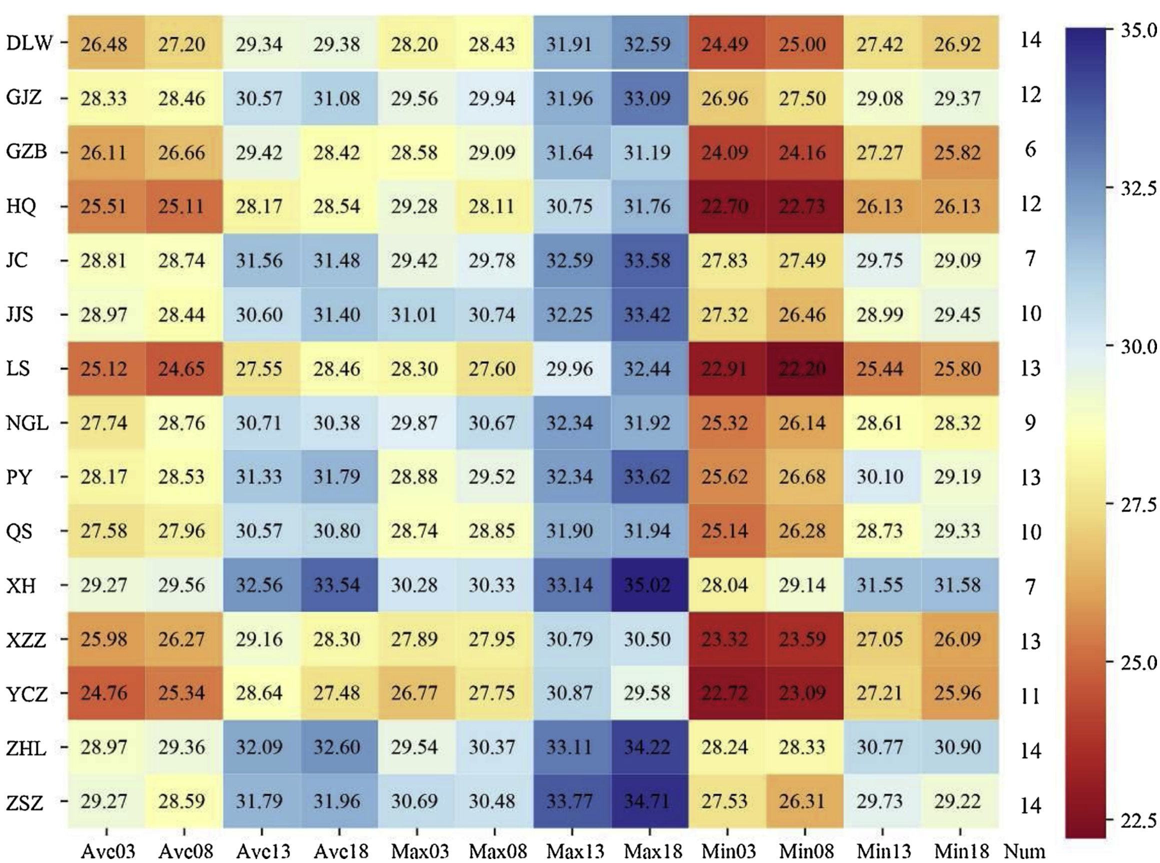

Fig. 5. Land surface temperature (LST) values of studied streets in 2003, 2 008, 2013, and 2018.
DLW, DLW, GJZ… represents street name abbreviations; Ave, Max, and Min represent the average, maximum, and minimum values of each streets' LST; Num represents the number of communities in each street.

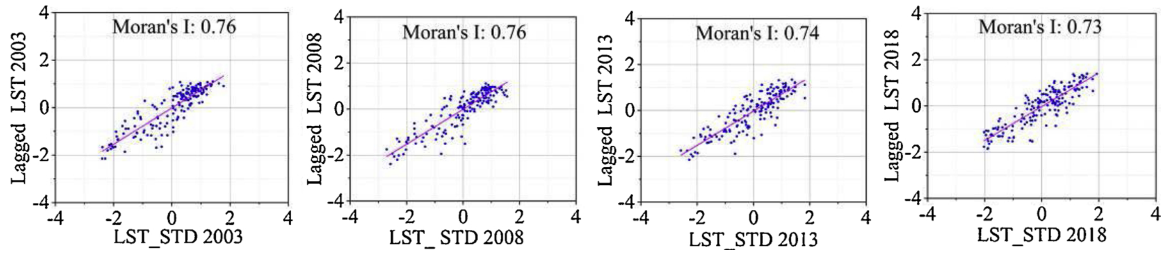

Fig. 6. Moran scatter plot of land surface temperature (LST) in the Ganjingzi area for each time period (2003, 2008, 2013, and 2018).

dependent variable and 16 independent variables used as predictors in the regression analysis. To ensure that the data were normally distributed and to avoid multicollinearity, logarithmic processing was concurrently performed on the data on both sides of the equation before performing the regression analysis.

Table 4 shows that the SEM model has higher R^2 and Logl values, lower AIC and SC. The R^2 and LogL values were 0.871 and 354.517, respectively; the AIC and SC values were -675.037 and -622.236, respectively. By comparing the R^2, AIC, SC, and LogL values of the three models, the SEM model is better than the SLM and OLS models. Thus, SEM was chosen as the explanatory model.

4. Discussion

4.1. Influence of urban spatial form on LST

Currently, scholars are limited to a single factor in the exploration of surface temperature driving factors, such as population density, land use and a landscape index, a remote sensing spectral index (NDBI, NDVI, NDSI), or three-dimensional architecture. Correlation methods are used to analyze the relationship between the impact factor and LST, ignoring the influence of other elements of urban interior space on thermal environmental elements (Chen & Zhang, 2017; Yang et al., 2018). The city is a center of human activities and a complex socio-economic-natural ecosystem. Changes in surface temperature characteristics are influenced by many factors in the urban two-dimensional and three-dimensional space (Berger et al., 2017; Deilami, Kamruzzaman, & Liu, 2018). Three-dimensional structures, land use, landscape metrics, socioeconomics, topography, and remote sensing indices all influence LSTs. Therefore, exploring the relationship between driving factors and surface temperature through spatial statistical methods is of significance. Table 3 shows the relationships among driving factors to LST by community in which, the correlation for building form is lower than that for social economy, topography, landscape index, and land use type.

To further illustrate the effects of land use, landscape metrics, socioeconomic characteristics, and topography on LST, we generated

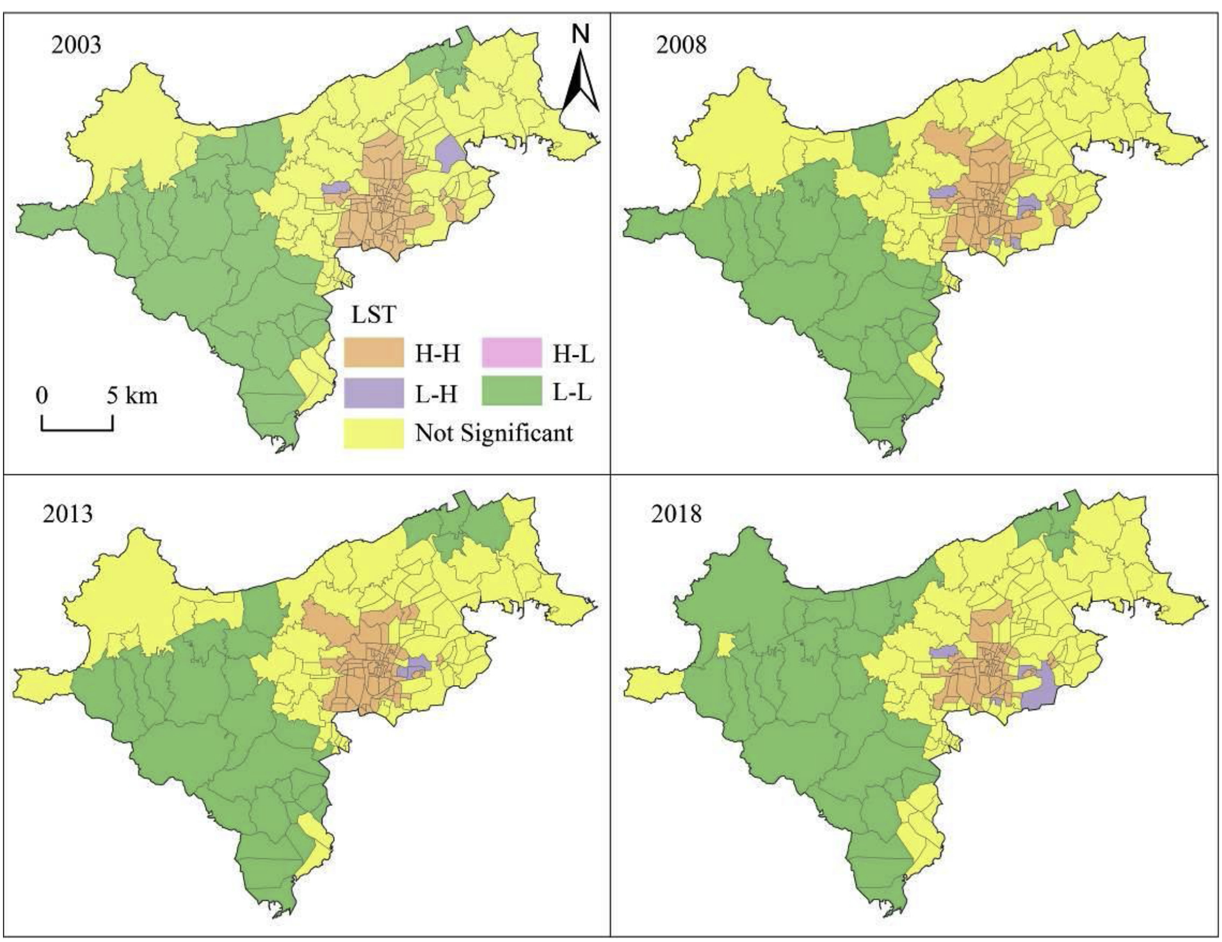

Fig. 7. Spatial distribution/agglomeration of land surface temperatures (LSTs) in 2003, 2008, 2013, and 2018.

Table 4
Comparative results among the OLS, SEM, and SLM regression analyses.

Type	Variable	OLS	SLM	SEM
	Intercept	11.571	11.391	13.587
Building form	Ln*BD*	−0.003 (−0.834)	−0.003 (−1.219)	−0.000 (−0.192)
	Ln*SVF*	0.412 (1.886)	0.419 (1.549)	0.521 (1.996)
Land use	Ln*PCL*	0.020 (2.613)	0.021 (2.448)	0.033 (3.847)
	Ln*PWG*	−0.007 (−3.306)	−0.008 (−3.056)	−0.008 (−2.971)
	Ln*PW*	−0.007 (−2.550)	−0.006 (−2.612)	−0.007 (−3.131)
Landscape index	Ln*PD*	−0.004 (−0.834)	−0.004 (−0.979)	−0.001 (−0.291)
	Ln*AI*	−1.844 (−1.185)	−1.777 (−1.140)	−2.295 (−1.488)
	Ln*LPI*	0.020 (1.830)	0.020 (1.626)	0.012 (0.987)
Socioeconomic	Ln*NL*	0.012 (2.835)	0.012 (2.667)	0.008 (1.711)
	Ln*RD*	0.007 (2.024)	0.007 (1.854)	0.007 (1.924)
	Ln*DisW*	0.008 (1.873)	0.009 (1.860)	0.012 (2.486)
Terrain	Ln*DEM*	−0.006 (−0.818)	−0.007 (−0.901)	−0.011 (−1.395)
	Ln*Slope*	0.016 (1.718)	0.017 (1.655)	0.021 (1.994)
Remote sensing index	Ln*NDVI*	−0.091 (−4.883)	−0.094 (−5.151)	−0.093 (−1.395)
	Ln*NDBI*	−0.001 (−0.126)	−0.001 (−0.049)	−0.000 (−0.036)
	Ln*NDSI*	−0.002 (0.600)	−0.002 (−0.611)	−0.004 (−1.342)
Test coefficient	R^2	0.8647	0.8649	0.871
	AIC	−664.319	−669.266	−675.037
	SC	−618.203	−613.359	−622.236
	LogL	352.502	352.633	354.517

Note: (The data in parentheses is the statistical value of t).

boxplots for each variable (Fig. 8). Land-use types were found to be strongly related to LST, and LST by land-use type could be subcategorized as built-up, agricultural, forest, grassland, bodies of water, or other types of land. The higher the AI and LPI landscape metrics, the higher the LST; the larger the PD value, the lower the LST value. The larger the NL, RD, and DisW values (socioeconomic characteristics), the steeper the LST increasing trend. The DEM had an important influence on LST; DEM values gradually increased within 60 m (Fig. 8). Along with increases in the DEM, LST value gradually decreased. Thus, multivariable analysis is needed for analyzing LSTs.

4.2. Influences on urban sustainability

As urbanization has advanced, the UHI effect has become a dominant feature of urban climates, which has significantly influenced residents' quality of life (Simwanda & Murayama, 2018; Sun, Gao, Li, Li, & Ma, 2018; Zhang et al., 2017; Zhao, He, Li, Wang, & Darko, 2017). Consequently, identifying ways to mitigate the effects of UHIs and promote sustainable urban development have been a continuous focus of urban planning and management. Based on previous research, this study examined the spatial characteristics of LSTs in Dalian City, China, including urban communities and their driving factors from the perspectives of spatial form, land use, landscape metrics, socioeconomics, topography, and remote sensing indices. These results are important for urban planning and land-use management in terms of improving the quality of the ecological environment and achieving sustainable development.

As a coastal city, Dalian City enjoys moderate temperatures in winter and summer and is a desirable residential location. However, recently, impervious land surfaces and high-rise buildings have gradually increased in Ganjingzi District while green space has decreased, somewhat degrading the ecological environment. For example, summer temperatures are slowly rising, which seriously affects quality of life. Rational planning for green space, transit, and land use is important for promoting the city's sustainable urban development.

4.3. Limitations

This paper explores the spatial and temporal differentiation characteristics and driving factors of LST at the community level through spatial statistical methods combined with many driving factors, which is of great significance to urban planning. However, this study has several limitations. Firstly, the study explored only the spatial characteristics of surface temperature in summer using LST spatiotemporal features; it did not consider the influence of seasonal and diurnal differences on LST spatial characteristics. Secondly, the study did not consider the influence of spatial scale on surface temperature and ignored the relationship between thermal environmental characteristics and driving factors at different scales. Finally, limited by data acquisition, the spatial measurement method was only used to explore the relationship between LST and driving factors over a single time period, and the relationship between driving factors and LST in each time period was not compared. Therefore, examining the differences in surface temperature at different scales, seasons, and times of day using panel data to explore the relationship between LST and many driving factors will be the focus of follow-up research.

5. Conclusions

This study used a mono-window algorithm to invert LST at the community level, followed by spatial autocorrelation and a spatial regression model to examine spatiotemporal LST patterns and their driving factors in terms of spatial form, land use, landscape metrics, socioeconomics, topography, and remote sensing indices. The main conclusions derived from the analytical results are as follows.

1 Between 2003 and 2018, LSTs in the studied communities gradually increased. Communities with high LSTs were concentrated in the middle of the study area, where the dominant land use type is built-up. Southern and western areas were influenced by factors such as topography and proximity to the sea, and consequently had lower LSTs.
2 From the perspective of global and local LST autocorrelations, the LSTs of the four periods had relatively high Moran's I values, indicating significantly positive spatial correlations. Among them, H-H and L-L values were concentrated in the central and southwestern areas of the study area, respectively.
3 LSTs' spatial characteristics were driven by many factors, and the land-use type, landscape metrics, and remote sensing indices had the strongest correlations, followed by nighttime light and socioeconomic characteristics; spatial form was weakly correlated. SEM was used to analyze the influences of the driving factors on LST because, where the spatial metric model was used, SEM offered the best fit to the data.

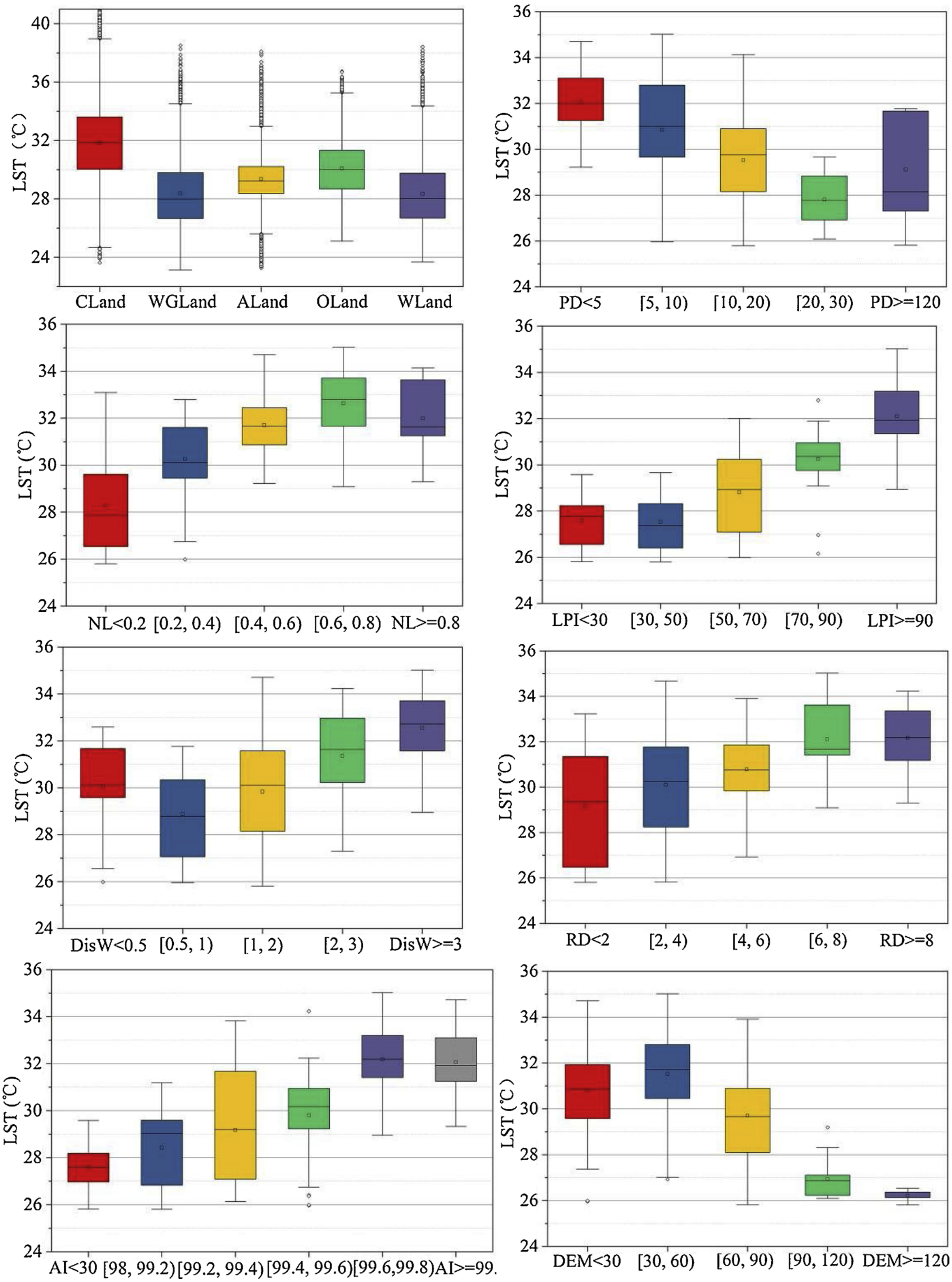

Fig. 8. Influences on land surface temperatures (LSTs).

Declaration of Competing Interest

This manuscript has not been published or presented elsewhere in part or in entirety and is not under consideration by another journal. We have read and understood your journal's policies, and we believe that neither the manuscript nor the study violates any of these. There are no conflicts of interest to declare.

Acknowledgments

This research study was supported by the National Natural Science Foundation of China (grant no. 41771178, 41630749), Innovative Talents Support Program of Liaoning Province (Grant No. LR2017017). The authors would like to acknowledge all experts' contributions in the building of the model and the formulation of the strategies in this study.

References

Anselin, L., & Rey, S. (1991). Properties of tests for spatial dependence in linear regression models. *Geographical Analysis, 23*(2), 112–131. https://doi.org/10.1111/j.1538-4632.1991.tb00228.x.

Azhdari, A., Soltani, A., & Alidadi, M. (2018). Urban morphology and landscape structure effect on land surface temperature: Evidence from Shiraz, a semi-arid city. *Sustainable Cities and Society, 41*, 853–864. https://doi.org/10.1016/j.scs.2018.06.034.

Berger, C., Rosentreter, J., Voltersen, M., Baumgart, C., Schmullius, C., & Hese, S. (2017). Spatio-temporal analysis of the relationship between 2D/3D urban site characteristics and land surface temperature. *Remote Sensing of Environment, 193*, 225–243. https://doi.org/10.1016/j.rse.2017.02.020.

Bolund, P., & Hunhammar, S. (1999). Ecosystem services in urban areas. *Ecological Economics, 29*(2), 293–301. https://doi.org/10.1016/S0921-8009(99)00013-0.

Cai, M., Ren, C., Xu, Y., Lau, K. K., & Wang, R. (2018). Investigating the relationship between local climate zone and land surface temperature using an improved WUDAPT methodology-A case study of Yangtze River Delta, China. *Urban Climate, 24*, 485–502. https://doi.org/10.1016/j.uclim.2017.05.010.

Chen, F., Yang, X., & Zhu, W. (2014). WRF simulations of urban heat island under hot-weather synoptic conditions: The case study of Hangzhou City, China. *Atmospheric Research, 138*, 364–377. https://doi.org/10.1016/j.atmosres.2013.12.005.

Chen, X., Zhao, H., Li, P., & Yin, Z. (2006). Remote sensing image-based analysis of the relationship between urban heat island and land use/cover changes. *Remote Sensing of Environment, 104*(2), 133–146. https://doi.org/10.1016/j.rse.2005.11.016.

Chen, X., & Zhang, Y. (2017). Impacts of urban surface characteristics on spatiotemporal pattern of land surface temperature in Kunming of China. *Sustainable Cities and Society, 32*, 87–99. https://doi.org/10.1016/j.scs.2017.03.013.

Chun, B., & Guldmann, J. M. (2014). Spatial statistical analysis and simulation of the urban heat island in high-density central cities. *Landscape and Urban Planning, 125*, 76–88. https://doi.org/10.1016/j.landurbplan.2014.01.016.

Cristóbal, J., Jiménez-Muñoz, J., Prakash, A., Mattar, C., Skoković, D., & Sobrino, J. (2018). An improved single-channel method to retrieve land surface temperature from the Landsat-8 Thermal Band. *Remote Sensing, 10*(3), 431. https://doi.org/10.3390/rs10030431.

Dai, Z., Guldmann, J., & Hu, Y. (2018). Spatial regression models of park and land-use impacts on the urban heat island in central Beijing. *Science of the Total Environment, 626*, 1136–1147. https://doi.org/10.1016/j.scitotenv.2018.01.165.

Deilami, K., Kamruzzaman, M., & Liu, Y. (2018). Urban heat island effect: A systematic review of spatio-temporal factors, data, methods, and mitigation measures. *International Journal of Applied Earth Observation and Geoinformation, 67*, 30–42. https://doi.org/10.1016/j.jag.2017.12.009.

Dwivedi, A., & Khire, M. V. (2018). Application of split-window algorithm to study Urban Heat Island effect in Mumbai through land surface temperature approach. *Sustainable Cities and Society, 41*, 865–877. https://doi.org/10.1016/j.scs.2018.02.030.

Feng, Y., Gao, C., Tong, X., Chen, S., Lei, Z., & Wang, J. (2019). Spatial Patterns of Land Surface Temperature and Their Influencing Factors: A Case Study in Suzhou, China. *Remote Sensing, 11*(2), 182. https://doi.org/10.3390/rs11020182.

Gage, E. A., & Cooper, D. J. (2017). Relationships between landscape pattern metrics, vertical structure and surface urban Heat Island formation in a Colorado suburb. *Urban Ecosystems, 20*(6), 1229–1238. https://doi.org/10.1007/s11252-017-0675-0.

He, B. (2018). Potentials of meteorological characteristics and synoptic conditions to mitigate urban heat island effects. *Urban Climate, 24*, 26–33. https://doi.org/10.1016/j.uclim.2018.01.004.

He, B., Zhao, Z., Shen, L., Wang, H., & Li, L. (2019). An approach to examining performances of cool/hot sources in mitigating/enhancing land surface temperature under different temperature backgrounds based on landsat 8 image. *Sustainable Cities and Society, 44*, 416–427. https://doi.org/10.1016/j.scs.2018.10.049.

Howard, L. (1818). *The climate of London, Vol. 1* W. Phillips, sold also by J. and A. Arch.

Imhoff, M. L., Zhang, P., Wolfe, R. E., & Bounoua, L. (2010). Remote sensing of the urban heat island effect across biomes in the continental USA. *Remote Sensing of Environment, 114*(3), 504–513. https://doi.org/10.1016/j.rse.2009.10.008.

KIM, H. H. (1992). Urban heat island. *International Journal of Remote Sensing, 13*(12), 2319–2336. https://doi.org/10.1080/01431169208904271.

Kong, L., Lau, K. K., Yuan, C., Chen, Y., Xu, Y., Ren, C., et al. (2017). Regulation of outdoor thermal comfort by trees in Hong Kong. *Sustainable Cities and Society, 31*, 12–25. https://doi.org/10.1016/j.scs.2017.01.018.

Li, J., Song, C., Cao, L., Zhu, F., Meng, X., & Wu, J. (2011). Impacts of landscape structure on surface urban heat islands: A case study of Shanghai, China. *Remote Sensing of Environment, 115*(12), 3249–3263. https://doi.org/10.1016/j.rse.2011.07.008.

Li, S., Zhao, Z., Miaomiao, X., & Wang, Y. (2010). Investigating spatial non-stationary and scale-dependent relationships between urban surface temperature and environmental factors using geographically weighted regression. *Environmental Modelling & Software, 25*(12), 1789–1800. https://doi.org/10.1016/j.envsoft.2010.06.011.

Li, X., Zhou, W., Ouyang, Z., Xu, W., & Zheng, H. (2012). Spatial pattern of greenspace affects land surface temperature: evidence from the heavily urbanized Beijing metropolitan area, China. *Landscape Ecology, 27*(6), 887–898. https://doi.org/10.1007/s10980-012-9731-6.

Luo, X., & Peng, Y. (2016). Scale effects of the relationships between Urban Heat Islands and impact factors based on a geographically-weighted regression model. *Remote Sensing, 8*(9), 760. https://doi.org/10.3390/rs8090760.

Mathew, A., Khandelwal, S., Kaul, N., & Chauhan, S. (2018). Analyzing the diurnal variations of land surface temperatures for surface urban heat island studies: Is time of observation of remote sensing data important? *Sustainable Cities and Society, 40*, 194–213. https://doi.org/10.1016/j.scs.2018.03.032.

Mathew, A., Khandelwal, S., & Kaul, N. (2017). Investigating spatial and seasonal variations of urban heat island effect over Jaipur city and its relationship with vegetation, urbanization and elevation parameters. *Sustainable Cities and Society, 35*, 157–177. https://doi.org/10.1016/j.scs.2017.07.013.

Mirzaei, P. A. (2015). Recent challenges in modeling of urban heat island. *Sustainable Cities and Society, 19*, 200–206. https://doi.org/10.1016/j.scs.2015.04.001.

Mirzaei, P. A., & Haghighat, F. (2010). Approaches to study urban heat island-abilities and limitations. *Building and Environment, 45*(10), 2192–2201. https://doi.org/10.1016/j.buildenv.2010.04.001.

Ngie, A., Abutaleb, K., Ahmed, F., Darwish, A., & Ahmed, M. (2014). Assessment of urban heat island using satellite remotely sensed imagery: A review. *South African Geographical Journal, 96*(2), 198–214. https://doi.org/10.1080/03736245.2014.924864.

Oke, T. R. (1982). The energetic basis of the urban heat island. *Quarterly Journal of the Royal Meteorological Society, 108*(455), 1–24. https://doi.org/10.1002/qj.49710845502.

Peng, J., Ma, J., Liu, Q., Liu, Y., Hu, Y., Li, Y., et al. (2018). Spatial-temporal change of land surface temperature across 285 cities in China: An urban-rural contrast perspective. *Science of the Total Environment, 635*, 487–497. https://doi.org/10.1016/j.scitotenv.2018.04.105.

Qiao, Z., Tian, G., & Xiao, L. (2013). Diurnal and seasonal impacts of urbanization on the urban thermal environment: A case study of Beijing using MODIS data. *ISPRS Journal of Photogrammetry and Remote Sensing, 85*, 93–101. https://doi.org/10.1016/j.isprsjprs.2013.08.010.

Qin, Z., Karnieli, A., & Berliner, P. (2001). A mono-window algorithm for retrieving land surface temperature from Landsat TM data and its application to the Israel-Egypt border region. *International Journal of Remote Sensing, 22*(18), 3719–3746. https://doi.org/10.1080/01431160010006971.

Qu, B., Zhu, W., Jia, S., & Lv, A. (2015). Spatio-temporal changes in vegetation activity and its driving factors during the growing season in China from 1982 to 2011. *Remote Sensing, 7*(10), 13729–13752. https://doi.org/10.3390/rs71013729.

Ren, C., Ng, E. Y. Y., & Katzschner, L. (2011). Urban climatic map studies: A review. *International Journal of Climatology, 31*(15), 2213–2233. https://doi.org/10.1002/joc.2237.

Rizwan, A. M., Dennis, L. Y., & Chunho, L. (2008). A review on the generation, determination and mitigation of Urban Heat Island. *Journal of Environmental Sciences, 20*(1), 120–128.

Scarano, M., & Mancini, F. (2017). Assessing the relationship between sky view factor and land surface temperature to the spatial resolution. *International Journal of Remote Sensing, 38*(23), 6910–6929. https://doi.org/10.1080/01431161.2017.1368099.

Shi, Y., Katzschner, L., & Ng, E. (2018). Modelling the fine-scale spatiotemporal pattern of urban heat island effect using land use regression approach in a megacity. *Science of the Total Environment, 618*, 891–904. https://doi.org/10.1016/j.scitotenv.2017.08.252.

Simwanda, M., & Murayama, Y. (2018). Spatiotemporal patterns of urban land use change in the rapidly growing city of Lusaka, Zambia: Implications for sustainable urban development. *Sustainable Cities and Society, 39*, 262–274. https://doi.org/10.1016/j.scs.2018.01.039.

Singh, P., Kikon, N., & Verma, P. (2017). Impact of land use change and urbanization on urban heat island in Lucknow city, Central India. A remote sensing based estimate. *Sustainable Cities and Society, 32*, 100–114. https://doi.org/10.1016/j.scs.2017.02.018.

Sobrino, J. A., Jiménez-Muñoz, J. C., & Paolini, L. (2004). Land surface temperature retrieval from LANDSAT TM 5. *Remote Sensing of Environment, 90*(4), 434–440. https://doi.org/10.1016/j.rse.2004.02.003.

Sobrino, J. A., Li, Z. L., Stoll, M. P., & Becker, F. (1996). Multi-channel and multi-angle algorithms for estimating sea and land surface temperature with ATSR data. *International Journal of Remote Sensing, 17*(11), 2089–2114. https://doi.org/10.1080/01431169608948760.

Son, N., & Thanh, B. (2018). Decadal assessment of urban sprawl and its effects on local temperature using Landsat data in Cantho city, Vietnam. *Sustainable Cities and Society, 36*, 81–91. https://doi.org/10.1016/j.scs.2017.10.010.

Song, J., Du, S., Feng, X., & Guo, L. (2014). The relationships between landscape compositions and land surface temperature: Quantifying their resolution sensitivity with spatial regression models. *Landscape and Urban Planning, 123*, 145–157. https://doi.org/10.1016/j.landurbplan.2013.11.014.

Stewart, I. D., & Oke, T. R. (2012). Local climate zones for urban temperature studies. *Bulletin of the American Meteorological Society, 12*(93), 1879–1900. https://doi.org/10.1175/BAMS-D-11-00019.1.

Stone, B., Jr, & Rodgers, M. O. (2001). Urban form and thermal efficiency: How the design of cities influences the urban heat island effect. *American Planning Association. Journal of the American Planning Association, 67*(2), 186. https://doi.org/10.1080/01944360108976228.

Sun, Y., Gao, C., Li, J., Li, W., & Ma, R. (2018). Examining urban thermal environment dynamics and relations to biophysical composition and configuration and socio-economic factors: A case study of the Shanghai metropolitan region. *Sustainable Cities and Society, 40*, 284–295. https://doi.org/10.1016/j.scs.2017.12.004.

Tan, J., Zheng, Y., Tang, X., Guo, C., Li, L., Song, G., et al. (2010). The urban heat island and its impact on heat waves and human health in Shanghai. *International Journal of Biometeorology, 54*(1), 75–84. https://doi.org/10.1007/s00484-009-0256-x.

Tobler, W. R. (1970). A computer movie simulating urban growth in the Detroit region. *Economic Geography, 46*(sup1), 234–240.

Valor, E., & Caselles, V. (1996). Mapping land surface emissivity from NDVI: Application to European, African, and South American areas. *Remote Sensing of Environment, 57*(3), 167–184. https://doi.org/10.1016/0034-4257(96)00039-9.

Voogt, J. A., & Oke, T. R. (2003). Thermal remote sensing of urban climates. *Remote Sensing of Environment, 86*(3), 370–384. https://doi.org/10.1016/s0034-4257(03)

00079-8.
Wan, Z., & Dozier, J. (1996). A generalized split-window algorithm for retrieving land-surface temperature from space. *IEEE Transactions on Geoscience and Remote Sensing, 34*(4), 892–905. https://doi.org/10.1109/36.508406.
Wang, F., Qin, Z., Song, C., Tu, L., Karnieli, A., & Zhao, S. (2015). An improved mono-window algorithm for land surface temperature retrieval from Landsat 8 thermal infrared sensor data. *Remote Sensing, 7*(4), 4268–4289. https://doi.org/10.3390/rs70404268.
Wang, S., Ma, Q., Ding, H., & Liang, H. (2018). Detection of urban expansion and land surface temperature change using multi-temporal landsat images. *Resources, Conservation and Recycling, 128*, 526–534. https://doi.org/10.1016/j.resconrec.2016.05.011.
Wang, W. C., Zeng, Z., & Karl, T. R. (1990). Urban heat islands in China. *Geophysical Research Letters, 17*(13), 2377–2380. https://doi.org/10.1029/gl017i013p02377.
Wang, W., Liang, S., & Meyers, T. (2008). Validating MODIS land surface temperature products using long-term nighttime ground measurements. *Remote Sensing of Environment, 112*(3), 623–635.
Wei, C., Yao, Z., Chongyu, P., & Weijun, G. (2017). Evaluation of urbanization dynamics and its impacts on surface heat islands: A case study of Beijing, China. *Remote Sensing, 9*(5), 453. https://doi.org/10.3390/rs9050453.
Yang, G., Pu, R., Zhao, C., Huang, W., & Wang, J. (2011). Estimation of subpixel land surface temperature using an endmember index based technique: A case examination on ASTER and MODIS temperature products over a heterogeneous area. *Remote Sensing of Environment, 115*(5), 1202–1219. https://doi.org/10.1016/j.rse.2011.01.004.
Yang, J., Jin, S., Xiao, X., Jin, C., Xia, J. C., Li, X., et al. (2019). Local climate zone ventilation and urban land surface temperatures: Towards a performance-based and wind-sensitive planning proposal in megacities. *Sustainable Cities and Society, 47*, 101487. https://doi.org/10.1016/j.scs.2019.101487.
Yang, J., Su, J., Xia, J. C., Jin, C., Li, X., & Ge, Q. (2018). The impact of spatial form of urban architecture on the urban thermal environment: A case study of the Zhongshan District, Dalian, China. *IEEE Journal of Selected Topics in Applied Earth Observations and Remote Sensing, 11*(8), 2709–2716. https://doi.org/10.1109/JSTARS.2018.2808469.
Yang, J., Wang, Y., Xiao, X., Jin, C., Xia, J. C., & Li, X. (2019). Spatial differentiation of urban wind and thermal environment in different grid sizes. *Urban Climate, 28*, 100458. https://doi.org/10.1016/j.uclim.2019.100458.
Yang, X., Ruby Leung, L., Zhao, N., Zhao, C., Qian, Y., Hu, K., et al. (2017). Contribution of urbanization to the increase of extreme heat events in an urban agglomeration in east China. *Geophysical Research Letters, 44*(13), 6940–6950. https://doi.org/10.1002/2017GL074084.
Yin, C., Yuan, M., Lu, Y., Huang, Y., & Liu, Y. (2018). Effects of urban form on the urban heat island effect based on spatial regression model. *Science of the Total Environment, 634*, 696–704. https://doi.org/10.1016/j.scitotenv.2018.03.350.
Yue, W., Liu, Y., Fan, P., Ye, X., & Wu, C. (2012). Assessing spatial pattern of urban thermal environment in Shanghai, China. *Stochastic Environmental Research and Risk Assessment, 26*(7), 899–911. https://doi.org/10.1007/s00477-012-0638-1.
Yue, W., Xu, J., Tan, W., & Xu, L. (2007). The relationship between land surface temperature and NDVI with remote sensing: Application to Shanghai Landsat 7 ETM+ data. *International Journal of Remote Sensing, 28*(15), 3205–3226. https://doi.org/10.1080/01431160500306906.
Zakšek, K., Oštir, K., & Kokalj (2011). Sky-view factor as a relief visualization technique. *Remote Sensing, 3*(2), 398–415. https://doi.org/10.3390/rs3020398.
Zhang, X., Estoque, R. C., & Murayama, Y. (2017). An urban heat island study in Nanchang City, China based on land surface temperature and social-ecological variables. *Sustainable Cities and Society, 32*, 557–568. https://doi.org/10.1016/j.scs.2017.05.005.
Zhao, C., Jensen, J., Weng, Q., & Weaver, R. (2018). A geographically weighted regression analysis of the underlying factors related to the surface urban heat island phenomenon. *Remote Sensing, 10*(9), 1428. https://doi.org/10.3390/rs10091428.
Zhao, M., Cai, H., Qiao, Z., & Xu, X. (2016). Influence of urban expansion on the urban heat island effect in Shanghai. *International Journal of Geographical Information Science, 30*(12), 2421–2441. https://doi.org/10.1080/13658816.2016.1178389.
Zhao, Z., He, B., Li, L., Wang, H., & Darko, A. (2017). Profile and concentric zonal analysis of relationships between land use/land cover and land surface temperature: Case study of Shenyang, China. *Energy and Buildings, 155*, 282–295. https://doi.org/10.1016/j.enbuild.2017.09.046.
Zhou, X., & Chen, H. (2018). Impact of urbanization-related land use land cover changes and urban morphology changes on the urban heat island phenomenon. *Science of the Total Environment, 635*, 1467–1476. https://doi.org/10.1016/j.scitotenv.2018.04.091.
Zullo, F., Fazio, G., Romano, B., Marucci, A., & Fiorini, L. (2019). Effects of urban growth spatial pattern (UGSP) on the land surface temperature (LST): A study in the Po Valley (Italy). *Science of the Total Environment, 650*, 1740–1751. https://doi.org/10.1016/j.scitotenv.2018.09.331.